EDGE ARTICLE

Check for updates

All publication charges for this article
have been paid for by the Royal Society
of Chemistry

Ligand-induced changes in the electrocatalytic activity of atomically precise Au$_{25}$ nanoclusters†

Lipan Luo,‡[a] Xia Zhou,‡[b] Yuping Chen,[a] Fang Sun,[a] Likai Wang [iD] *[b]
and Qing Tang [iD] *[a]

Atomically precise gold nanoclusters have shown great promise as model electrocatalysts in pivotal electrocatalytic processes such as the hydrogen evolution reaction (HER) and carbon dioxide reduction reaction (CO$_2$RR). Although the influence of ligands on the electronic properties of these nanoclusters is well acknowledged, the ligand effects on their electrocatalytic performances have been rarely explored. Herein, using [Au$_{25}$(SR)$_{18}$]$^-$ nanoclusters as a prototype model, we demonstrated the importance of ligand hydrophilicity *versus* hydrophobicity in modulating the interface dynamics and electrocatalytic performance. Our first-principles calculations revealed that Au$_{25}$ protected by hydrophilic –SCH$_2$COOH ligands exhibits faster kinetics in stripping the thiolate ligand and better HER activity due to enhanced proton transfer facilitated by boosted interface hydrogen bonding. Conversely, Au$_{25}$ protected by hydrophobic –SCH$_2$CH$_3$ ligands demonstrates enhanced CO$_2$RR performance by minimizing water interference to stabilize the key *COOH intermediate and lower the barrier for CO formation. Experimental validation using synthesized hydrophilic and hydrophobic ligand-protected Au$_{25}$ nanoclusters (NCs), such as [Au$_{25}$(MPA)$_{18}$]$^-$ (MPA = mercaptopropionic acid), [Au$_{25}$(MHA)$_{18}$]$^-$ (MHA = 6-mercaptohexanoic acid), and [Au$_{25}$(SC$_6$H$_{13}$)$_{18}$]$^-$, confirms these findings, where the hydrophilic ligand-protected Au$_{25}$ NCs exhibit better activity and stability in the HER, while the hydrophobic ligand-protected Au$_{25}$ NCs achieve higher faradaic efficiency and current density in the CO$_2$RR. The mechanistic insights in this study provide valuable guidance for the rational design of surface microenvironments in efficient nanocatalysts for sustainable energy applications.

1. Introduction

The electrocatalytic reactions such as the hydrogen evolution reaction (HER)[1–4] and carbon dioxide reduction reaction (CO$_2$RR) have been considered cornerstones in the pursuit of sustainable ways of meeting global energy demands.[5–7] These reactions are critical for the production of clean energy and recycling of carbon, as they enable the conversion of CO$_2$ into valuable chemicals and fuels and generate hydrogen as a clean energy carrier.[8,9] Given the importance of these processes, the development of highly efficient and stable catalysts for both the CO$_2$RR and HER is of paramount importance. Atomically precise metal nanoclusters (NCs), renowned for their unique structures and molecule-like properties, have shown exceptional catalytic capabilities due to their quantum confinement effects and a high density of active

sites.[10–18] Among these, [Au$_{25}$(SR)$_{18}$]$^-$ NCs have been particularly recognized for their significant electrocatalytic activities in both CO$_2$ reduction[12,19–22] and hydrogen evolution.[23–27] The pioneering work by Kauffman *et al.*[28] first highlighted the ability of [Au$_{25}$(SR)$_{18}$]$^-$ to efficiently reduce CO$_2$ to CO with high selectivity and low overpotential at commercially viable current densities, establishing the potential of these nanoclusters in electrocatalysis. The bimetallic PtAu$_{24}$(SR)$_{18}$ NCs, explored by Kwak *et al.*[29] demonstrated remarkable catalytic activity for hydrogen production in the HER, surpassing previously reported molecular catalysts and even outperforming traditional platinum catalysts, setting a new benchmark in the field.

In the context of Au$_{25}$ NCs, the choice and nature of ligands are critical factors that significantly influence their stability and catalytic performance. Ligands act as the outer protective layers, not only preventing aggregation and stabilizing the nanocluster, but also modulating its electronic properties and surface chemistry.[26,30–35] The thiol-based ligands, in particular, are widely used due to their strong S–metal bonds, which provide high stability and a straightforward preparation strategy.[36–38] However, beyond the stabilization effect, the intrinsic properties of the ligands—such as their hydrophilicity or hydrophobicity—can profoundly affect the nanocluster's interaction with reactants and

[a]School of Chemistry and Chemical Engineering, Chongqing Key Laboratory of Chemical Theory and Mechanism, Chongqing University, Chongqing 401331, China. E-mail: qingtang@cqu.edu.cn

[b]School of Chemistry and Chemical Engineering, Shandong University of Technology, Zibo, Shandong, 255049, China. E-mail: lkwangchem@sdut.edu.cn

† Electronic supplementary information (ESI) available. See DOI: https://doi.org/10.1039/d4sc07181f

‡ These two authors contributed equally to this work.

its overall electrocatalytic activity.[39] For instance, Kwak et al.[25] investigated the impact of different ligands on the HER performance and found that the 3-mercapto-1-propanesulfonic acid (MPS) protected Au_{25} NC achieved a rate constant of 121 000 s^{-1} at an overpotential of 0.7 V, which was 11 times higher than that of 1-hexanethiolate (C_6S) protected Au_{25}, highlighting the profound influence of ligand hydrophilicity on catalytic efficiency. Moreover, recent work by Yoo et al.[40] has shown that the introduction of hydrophobic ligands in a silver nanocluster Ag_{25} can enhance the CO_2 reduction activity, achieving a faradaic efficiency for CO (FE_{CO}) of over 90% and a partial current density (j_{CO}) as high as -240 mA cm^{-2} in a gas-fed membrane electrode assembly device. Despite these experimental advancements, atomic-level understanding and elucidation of the specific effects of hydrophilic versus hydrophobic ligands on the electrocatalytic performance of atomically precise NCs have been lacking. This uncertainty underscores the urgent need for a systematic investigation into how the ligand properties influence these catalytic processes. In particular, understanding these interactions is crucial for further optimizing the performance of Au_{25} NCs and could also provide valuable insights into the rational design of nanocluster-based electrocatalysts for sustainable energy applications.

In this work, we systematically investigated the ligand effect on the interface stability and the electrocatalytic performance of Au_{25} NCs in both acidic HER and alkaline CO_2RR processes. Utilizing hydrophilic $[Au_{25}(SCH_2COOH)_{17}]^-$ and hydrophobic $[Au_{25}(SCH_2CH_3)_{17}]^-$ NCs as theoretical models, we first explored how the ligand properties influence the Au–S interface dynamics, the electronic structures, and the electrocatalytic reaction kinetics via the constant potential calculations and ab initio molecular dynamics (AIMD) simulations. The results revealed that the Au–S interface is unstable at the applied electrochemical reduction potential, and hydrophilic $[Au_{25}(SCH_2COOH)_{17}]^-$ exhibits faster kinetics for the stripping of the –SR ligand. Moreover, in the acidic environment, hydrophilic Au_{25} NCs exhibit superior HER performance compared to the hydrophobic one due to the enhanced proton transfer and hydrogen evolution facilitated by the hydrophilic environment. Conversely, under alkaline conditions, hydrophobic Au_{25} NCs show better CO_2RR activity by promoting the adsorption and stabilization of CO_2 intermediates while minimizing the water interference around the reaction interface. Our theoretical predictions are then validated through the experimental studies, where we synthesized mercaptopropionic acid-protected $[Au_{25}(MPA)_{18}]^-$, 6-mercaptohexanoic acid-protected $[Au_{25}(MHA)_{18}]^-$, and hexanethiol-protected $[Au_{25}(SC_6H_{13})_{18}]^-$ NCs as model systems and performed the electrochemical tests. These insights provide a deeper understanding of how the ligand environments affect the electrocatalytic activities of Au_{25} nanoclusters and offer valuable guidance for the rational design of promising nanocatalysts for electrocatalytic applications.

2. Results and discussion

Ligand detachment dynamics

The removal of surface ligands from nanoclusters is a critical step in enhancing their electrocatalytic activity. Fully ligand-protected nanoclusters, such as $Au_{25}(SR)_{18}$, are typically considered electrochemically inactive and exhibit significant overpotential during the electrocatalytic process.[20,41–44] This inactivity is primarily caused by the passivating effect of the ligands, which block the access of reactants to the metal core and hinder the efficient mass and charge transfer between the nanocluster and the reactants.[45,46] Consequently, the selective removal of ligands from specific sites on the nanocluster surface is necessary to expose the active sites. Our recent studies have provided valuable insights into the mechanism of partial ligand removal in $Au_{25}(SCH_3)_{18}$ NCs, where the applied reduction potential would induce the spontaneous desulfurization process via breaking the Au–S bonds regardless of the electrolyte environment (acidic, neutral or basic conditions).[47]

Building on these prior findings, we first combined the constant potential calculations and AIMD simulations to explore how the presence of surface hydrophilic and hydrophobic ligands affects the stability of the Au–S interface under acidic electrochemical conditions. We modeled Au_{25} NCs with ligands aligned along the z-axis, simulating the system in both explicit water slabs and an implicit solvation environment to accurately capture the realistic electrochemical conditions. Our theoretical model includes hydrophilic $[Au_{25}(CH_2COOH)_{18}]^-$ and hydrophobic $[Au_{25}(CH_2CH_3)_{18}]^-$ NCs (illustrated in Fig. S2†) placed in the simulation box filled with bulk water at an average density of approximately 1 g cm^{-3}, which comprises 191 H_2O molecules and one H_3O^+ ion to simulate the acidic environment.[48] To explicitly consider the electrode potential, we manually adjusted the number of extra electrons to control the applied potential U (more details on the constant potential calculations can be found in the ESI†). Our AIMD simulations at room temperature (300 K) revealed that the –SR ligands on both the $[Au_{25}(CH_2COOH)_{18}]^-$ and $[Au_{25}(CH_2CH_3)_{18}]^-$ NCs become unstable when subjected to the applied potential. In the dynamic process, the proton from the solvated H_3O^+ ion is attracted and adsorbed onto the sulfur atom, weakening the Au–S bonds. When the potential becomes sufficiently negative, this weakening leads to the complete breakage of the Au–S bonds and the formation of the HSR molecule, as illustrated in the AIMD snapshots (Fig. 1, left). Specifically, in the case of $[Au_{25}(CH_2CH_3)_{18}]^-$ NCs, the potential ($U_{RHE} = -1.36$ V) was not negative enough to facilitate proton adsorption onto the sulfur atom, leading instead to proton transfer and diffusion into the solvent (details provided in Fig. S3†). In contrast, when a lower potential ($U_{RHE} = -1.54$ V) was applied, the Au–S bonds in $[Au_{25}(CH_2CH_3)_{18}]^-$ NCs were completely broken (Fig. 1b).

Fig. 1a illustrates the dynamic behavior of $[Au_{25}(SCH_2COOH)_{18}]^-$ NC at an applied potential of $U_{RHE} = -0.98$ V at 300 K in an acidic environment (pH = 0). The Au^1(surface)–S^{26} bond first rapidly breaks at around 0.12 ps with the spontaneous proton adsorption at the S site. The Au^8(staple)–S^{26} bond then breaks at 4.54 ps, which oscillates, reattaches, and completely breaks again at 7.25 ps, leading to bond dissociation thereafter. This eventually results in the detachment of two Au–S bonds, and in the meantime, the –SR ligand combines with a proton to desorb and dissolve into the solution as a $HSCH_2COOH$ molecule. A similar –SR detachment process occurs for
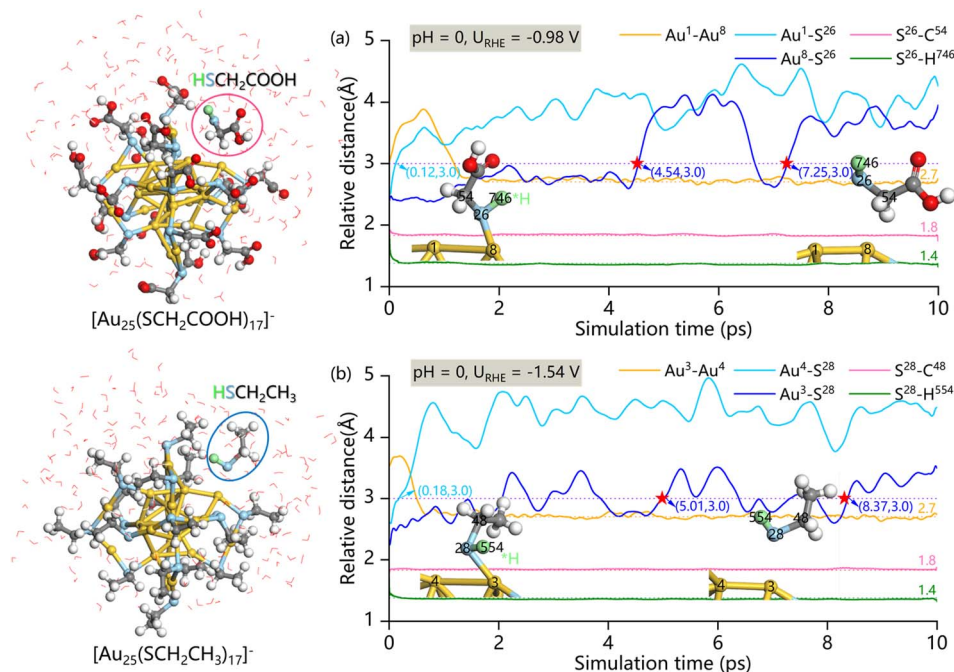
Fig. 1 Relative distances between representative atoms (marked with numbers) during the equilibrated AIMD simulations of (a) [Au$_{25}$(SCH$_2$-COOH)$_{18}$]$^-$ and (b) [Au$_{25}$(SCH$_2$CH$_3$)$_{18}$]$^-$ NCs at around 300 K and at an applied potential of −0.98 V for [Au$_{25}$(SCH$_2$COOH)$_{18}$]$^-$ and −1.54 V for [Au$_{25}$(SCH$_2$CH$_3$)$_{18}$]$^-$ in an acidic environment (pH = 0). The corresponding AIMD snapshots after 10 ps are shown on the left, while the insets (right) illustrate the local structures, highlighting the breaking of the Au(surface)−S and subsequent Au(staple)−S bonds. The water molecules in the water layer are shown in line mode. Color codes: yellow, Au; blue, S; grey, C; white, H from the ligand; green, the adsorbed H from the proton in solution. The same color scheme is used in the figures below.

[Au$_{25}$(SCH$_2$CH$_3$)$_{18}$]$^-$ at U_{RHE} = −1.54 V (Fig. 1b). The proton attack is accompanied by the rapid breaking of the Au^4(surface)−S^{28} bond at around 0.18 ps. Afterwards, the Au^3(staple)−S^{28} bond breaks at 5.01 ps and again at 8.37 ps, after which the ligand with adsorbed H dissolves into the solution as a free HSCH$_2$CH$_3$ molecule. Interestingly, it seems that the hydrophilic [Au$_{25}$(SCH$_2$COOH)$_{18}$]$^-$ NC exhibits faster etching dynamics in the process of ligand stripping. The faster dynamic process is further supported by the higher number of hydrogen bonds observed in the hydrophilic ligand-protected [Au$_{25}$(SCH$_2$COOH)$_{18}$]$^-$ system. Specifically, about 113 hydrogen bonds were formed with the surrounding 192 H$_2$O molecules, as shown in Fig. S4a,† compared to the 80 hydrogen bonds formed in the hydrophobic [Au$_{25}$(SCH$_2$CH$_3$)$_{18}$]$^-$ system. The increased hydrogen bonding in the hydrophilic system facilitates proton transfer to the sulfur atom, thus enhancing the kinetics of ligand detachment. To further investigate whether the carbon chain length of the ligands affects the interaction between the cluster and water molecules, we additionally conducted 10 ps dynamics simulations for Au$_{25}$ clusters protected by longer hydrophilic and hydrophobic ligands, [Au$_{25}$(MHA)$_{18}$]$^-$ (MHA = 6-mercaptohexanoic acid) and [Au$_{25}$(SC$_6$H$_{13}$)$_{18}$]$^-$, in the same water environment. The results showed that as the carbon chain length increases, the number of hydrogen bonds between the cluster and water molecules also increases. In the Au$_{25}$(MHA)$_{18}$ system, about 276 hydrogen bonds were formed, compared to 245 hydrogen bonds in Au$_{25}$(SC$_6$H$_{13}$)$_{18}$ (Fig. S4b†). Notably, the difference of 31 hydrogen bonds between the hydrophilic and

hydrophobic [Au$_{25}$(MHA)$_{18}$]$^-$ and [Au$_{25}$(SC$_6$H$_{13}$)$_{18}$]$^-$ is nearly identical to the 33 hydrogen bond difference observed in [Au$_{25}$(SCH$_2$COOH)$_{18}$]$^-$ and [Au$_{25}$(SCH$_2$CH$_3$)$_{18}$]$^-$. This similarity indicates that, although the total number of hydrogen bonds increases with longer carbon chains, the differences in hydrogen bond counts between Au$_{25}$ NCs with ligands of similar chain lengths are primarily attributed to the ligand hydrophilicity. Therefore, the accuracy of the simplified ligand calculations can be reliably ensured. These observations collectively underscore the critical role of applied potential, ligand environment, and hydrophilicity in driving the detachment of –SR ligands from the nanocluster surface—a necessary step for exposing active sites and enhancing the electrocatalytic performance of metal NCs.

HER performance in an acidic environment

Building on our above investigation into the dynamics of potential-induced ligand detachment, we now examine the electrocatalytic performance of the two dethiolated [Au$_{25}$(SR)$_{17}$]$^-$ structures, where one –SR ligand has been removed. To compare the HER performance of dethiolated [Au$_{25}$(SCH$_2$COOH)$_{17}$]$^-$ and [Au$_{25}$(SCH$_2$CH$_3$)$_{17}$]$^-$, we constructed models that include both the explicit solvation with 50 water molecules and the implicit solvation effects.[49] The HER testing was conducted under acidic conditions at pH = 0, providing an optimal environment for hydrogen evolution.

Fig. 2a and b present the U–ΔG plots derived from the work function fitting for [Au$_{25}$(SCH$_2$COOH)$_{17}$]$^-$ and

$[Au_{25}(SCH_2CH_3)_{17}]^-$, respectively. These plots were obtained by calculating the N_e–U and U–G relationships (additional details are provided in Fig. S5†). The results indicate that the first step of the HER, the Volmer reaction, is thermodynamically favorable across the entire potential range, as evidenced by ΔG values consistently below zero. This suggests that the adsorption of protons onto the nanocluster surface with exposed Au sites occurs spontaneously. However, the second step of the HER, the Heyrovsky reaction—which involves the formation of H_2— exhibits ΔG values greater than zero when the potential is not sufficiently negative. As the potential becomes more negative, the ΔG values gradually decrease, eventually falling below zero, indicating that the formation of H_2 becomes thermodynamically favorable only at more negative potentials. Therefore, these constant potential thermodynamic calculations lead us to conclude that, for both $[Au_{25}(SCH_2COOH)_{17}]^-$ and $[Au_{25}(SCH_2CH_3)_{17}]^-$, the formation of H_2 in the second step of the HER (Heyrovsky reaction) is the rate-determining step.

While thermodynamic calculations provide valuable insights into the feasibility of reaction steps, they often overlook the kinetic barriers that determine the rate at which these reactions proceed. To address this, we employed the slow-growth method within the framework of constrained kinetics to calculate the energy barriers associated with the rate-determining step of the HER for both $[Au_{25}(SCH_2COOH)_{17}]^-$ and $[Au_{25}(SCH_2CH_3)_{17}]^-$. Fig. 2c and d depict the energy barriers as a function of the constrained variable (CV) (Fig. S1†) at an applied potential of -0.66 V. As the constraint increases, the energy barrier

increases until it peaks at the point where two hydrogen atoms—one adsorbed at the Au bridge site and the other from H_3O^+ in the water environment—combine to form H_2 and then desorb. The analysis of the reaction pathway shows that the $[Au_{25}(SCH_2COOH)_{17}]^-$ system reaches this maximum energy barrier earlier, with a free energy of 0.42 eV, indicating a lower energy requirement for the rate-determining step. In contrast, at a similar potential, the energy barrier for the HER rate-determining step in the $[Au_{25}(SCH_2CH_3)_{17}]^-$ system is higher, at 0.54 eV. These results suggest that the hydrophilic $[Au_{25}(SCH_2COOH)_{17}]^-$ nanocluster exhibits superior HER performance compared to the hydrophobic $[Au_{25}(SCH_2COOH)_{17}]^-$ nanocluster. The lower kinetic barrier in the hydrophilic $[Au_{25}(SCH_2COOH)_{17}]^-$ system facilitates a more efficient hydrogen evolution reaction. This improved performance can be attributed to the enhanced interaction between the hydrophilic ligands and the surrounding aqueous environment, which promotes the formation and desorption of H_2, thereby making the HER process more favorable in $[Au_{25}(SCH_2COOH)_{17}]^-$.

CO$_2$RR performance in an alkaline environment

We further evaluated the CO$_2$RR performance of dethiolated $[Au_{25}(SCH_2COOH)_{17}]^-$ and $[Au_{25}(SCH_2CH_3)_{17}]^-$ by constant potential thermodynamic and kinetic calculations. The CO$_2$RR performance testing was carried out under alkaline conditions at pH = 14. Note that the alkaline environments are favorable
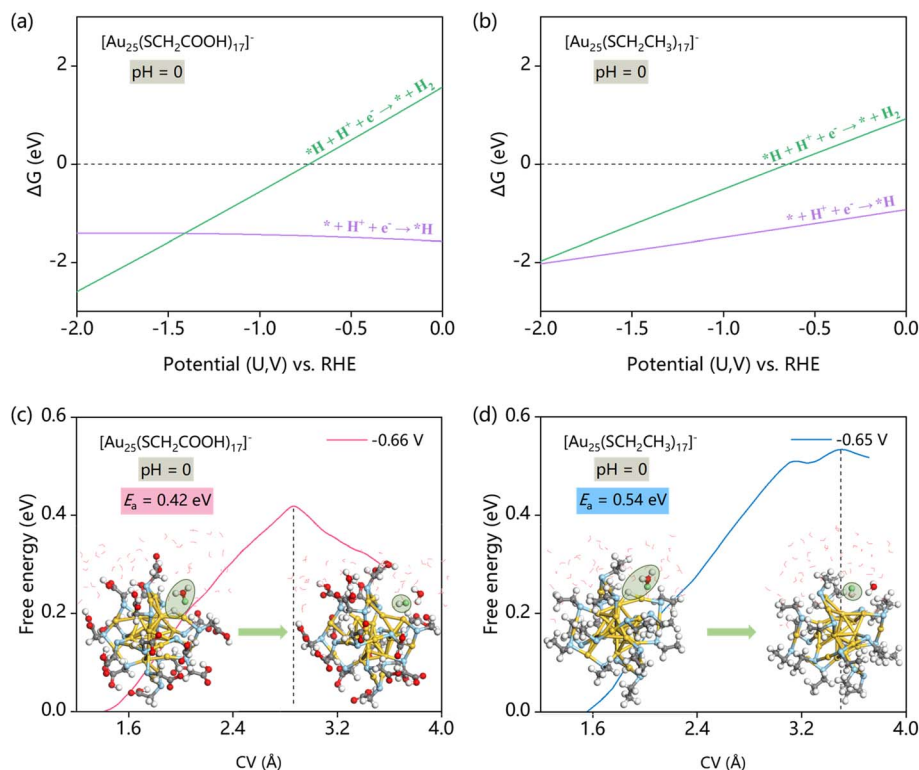

Fig. 2 Free energy changes (ΔG) for HER steps as a function of electrode potential for (a) $[Au_{25}(SCH_2COOH)_{17}]^-$ and (b) $[Au_{25}(SCH_2CH_3)_{17}]^-$. Energy profiles sampled by slow-growth (SG)-AIMD for the HER rate-determining step of (c) $[Au_{25}(SCH_2COOH)_{17}]^-$ and (d) $[Au_{25}(SCH_2CH_3)_{17}]^-$ at similar potentials (vs. RHE) with representative initial state (IS) and final state (FS) structures.

for CO_2 reduction and significantly suppress the HER, minimizing the interference and allowing for a more targeted comparison of CO_2RR activity between the two nanoclusters.

Fig. 3a and b show the U–ΔG plots derived from work function fitting for $[Au_{25}(SCH_2COOH)_{17}]^-$ and $[Au_{25}(SCH_2CH_3)_{17}]^-$, respectively (additional details are provided in Fig. S6†). These plots detail the ΔG values associated with the four key steps of the CO_2RR. Notably, the reaction of *COOH → *CO + OH$^-$ exhibits the highest ΔG value when the potential is higher than -1.0 V, indicating that it is the thermodynamically most challenging step. In contrast, the other three steps show lower ΔG values, suggesting that they are either spontaneous or more easily facilitated under the same potential conditions. Therefore, we conclude that the conversion of *COOH to *CO is the rate-determining step for the CO_2RR in both the nanocluster systems.

Next, we simulated the constant potential kinetics of this rate-determining step for both nanoclusters at similar applied potentials. As depicted in Fig. 3c and d, we tracked the energy barrier as a function of the constrained variable, which corresponds to the C–O bond distance within the *COOH intermediate (Fig. S1†). The energy barrier increases as the CV constraint grows, reaching a peak when *COOH is converted into *CO, and in the meantime, the generated OH$^-$ is released into the water environment. The kinetic analysis revealed that the energy barrier for the $[Au_{25}(SCH_2CH_3)_{17}]^-$ NC is relatively lower, with a smoother curve and a peak barrier of 0.76 eV. In contrast, the $[Au_{25}(SCH_2COOH)_{17}]^-$ NC exhibits a significantly higher energy barrier, with free energy peaking at 1.09 eV. This higher energy input indicates that the CO_2 reduction process in $[Au_{25}(SCH_2COOH)_{17}]^-$ is less efficient compared to that in $[Au_{25}(SCH_2CH_3)_{17}]^-$. The superior CO_2RR performance of $[Au_{25}(SCH_2CH_3)_{17}]^-$ can be attributed to the hydrophobic nature of the $-SCH_2CH_3$-protected nanocluster. The hydrophobic environment likely facilitates the desorption of the OH$^-$ species and the formation of *CO by minimizing interactions with the surrounding water molecules. This reduced interaction lowers the energy barrier for the rate-determining step, making the reaction pathway more favorable and thereby enhancing the overall CO_2 reduction efficiency.

To further substantiate the selectivity of the CO_2RR over the HER under alkaline conditions, we performed the constrained kinetic simulations for the competitive HER process on $[Au_{25}(SCH_2COOH)_{17}]^-$ and $[Au_{25}(SCH_2CH_3)_{17}]^-$ NCs. The results revealed that while the Volmer reaction (water dissociation and proton adsorption) is feasible (with a barrier less than 0.7 eV) (Fig. S7†), the Heyrovsky reaction (H_2 formation) encounters insurmountable barriers, where the splitting of the second H_2O molecule and subsequent H_2 generation display progressively increasing energy barriers (Fig. S8†). This indicates that the HER is kinetically hindered under alkaline conditions, thereby ensuring high selectivity for the CO_2RR on these nanoclusters.

The catalytic performance difference in the HER and CO_2RR

The optimized local structures of the Au(surface) and Au(staple) sites for both clusters are presented in Fig. 4a and b, while the
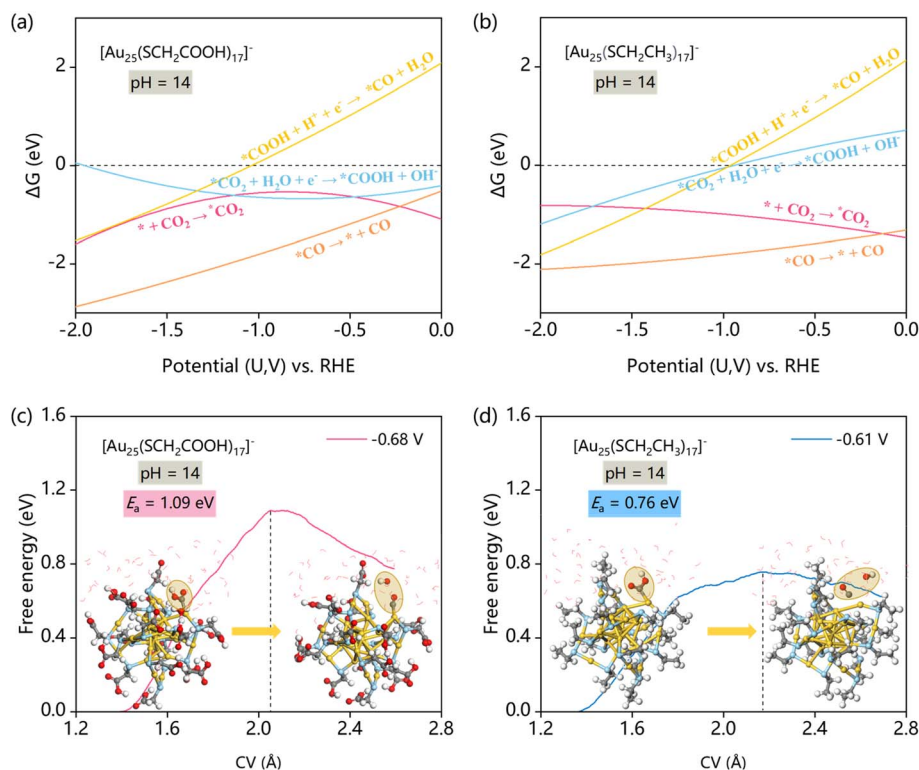

Fig. 3 Free energy changes (ΔG) for CO_2RR steps as a function of electrode potential for (a) $[Au_{25}(SCH_2COOH)_{17}]^-$ and (b) $[Au_{25}(SCH_2CH_3)_{17}]^-$. Energy profiles sampled by SG-AIMD for the rate-determining CO_2RR step of (c) $[Au_{25}(SCH_2COOH)_{17}]^-$ and (d) $[Au_{25}(SCH_2CH_3)_{17}]^-$ at similar potentials (vs. RHE) with representative IS and FS structures.

adsorption configurations of the key *H and *COOH intermediates are provided in Fig. S9.† Fig. 4c presents the radial distribution function (RDF) between the Au active sites in $[Au_{25}(SCH_2COOH)_{17}]^-$/$[Au_{25}(SCH_2CH_3)_{17}]^-$ and the hydrogen atoms of water molecules during the rate-determining steps of the HER and CO_2RR. The solid lines represent the RDF for both Au(surface) and Au(staple) during the HER, while the dashed lines depict the RDF for Au(staple) during the CO_2RR.

In the HER rate-determining step, the RDF considers both Au(staple) and Au(surface) sites because the *H adsorption occurs at both the active Au sites. The first RDF peak corresponds to the closest interactions between the Au atoms and the hydrogen atoms of surrounding water molecules, occurring around 1.7 Å. For $[Au_{25}(SCH_2COOH)_{17}]^-$, the $g(r)$ value at this peak is 3.25, whereas for $[Au_{25}(SCH_2CH_3)_{17}]^-$, it is significantly lower at 0.98. The higher $g(r)$ value for $[Au_{25}(SCH_2COOH)_{17}]^-$ indicates stronger and more frequent interactions between the Au active sites and the hydrogen atoms. This can be attributed to the hydrophilic nature of the $-SCH_2COOH$ ligands, which draw water molecules closer to the Au surface, enhancing proton transfer and interaction with active sites, thereby improving the HER performance. In contrast, the lower $g(r)$ value for $[Au_{25}(SCH_2CH_3)_{17}]^-$ reflects weaker interactions due to the hydrophobic nature of the $-SCH_2CH_3$ ligands, which repel water molecules and limit hydrogen bonding near the Au surface, thereby reducing the HER efficiency. The second RDF peak, occurring around 2.9 Å, reflects the next shell of water molecules interacting with the Au active sites. Here, the $g(r)$ value is 5.66 for $[Au_{25}(SCH_2COOH)_{17}]^-$ and 4.08 for $[Au_{25}(SCH_2CH_3)_{17}]^-$. The higher and sharper peak for the hydrophilic cluster indicates a more ordered and denser water structure around the Au atoms, which facilitates proton transfer and H_2 formation during the HER, further explaining its superior HER performance. Conversely, the less structured water network around the hydrophobic cluster hinders efficient proton transfer, limiting its HER activity.

For the CO_2RR rate-determining step, the RDF focuses on the interaction between Au(staple) and the hydrogen atoms of water molecules because $*CO_2$ and *COOH adsorption as well as the conversion to *CO occur exclusively at the Au(staple) site. Interestingly, $[Au_{25}(SCH_2COOH)_{17}]^-$ also shows a higher and sharper peak compared to $[Au_{25}(SCH_2CH_3)_{17}]^-$, indicating a more ordered and dense water structure around Au(staple). However, this structured water environment may hinder the adsorption and stabilization of CO_2RR intermediates such as *COOH by increasing the energy barrier for *COOH conversion to *CO. In contrast, the less structured water environment in $[Au_{25}(SCH_2CH_3)_{17}]^-$ minimizes water interference with CO_2RR intermediates, facilitating *COOH to *CO conversion with a lower barrier and enhancing CO_2RR performance.

Fig. 4d presents the Bader charge analysis of the Au(surface) and Au(staple) sites for both nanoclusters before and after the adsorption of key intermediates (*H and *COOH) in the HER and CO_2RR. These data reveal distinct differences in how the two systems interact with reactants, helping explain their differing catalytic performances. In the * state (without adsorption), both systems show similar Bader charges on the Au(surface) (0.13), but the Au(staple) in $[Au_{25}(SCH_2COOH)_{17}]^-$
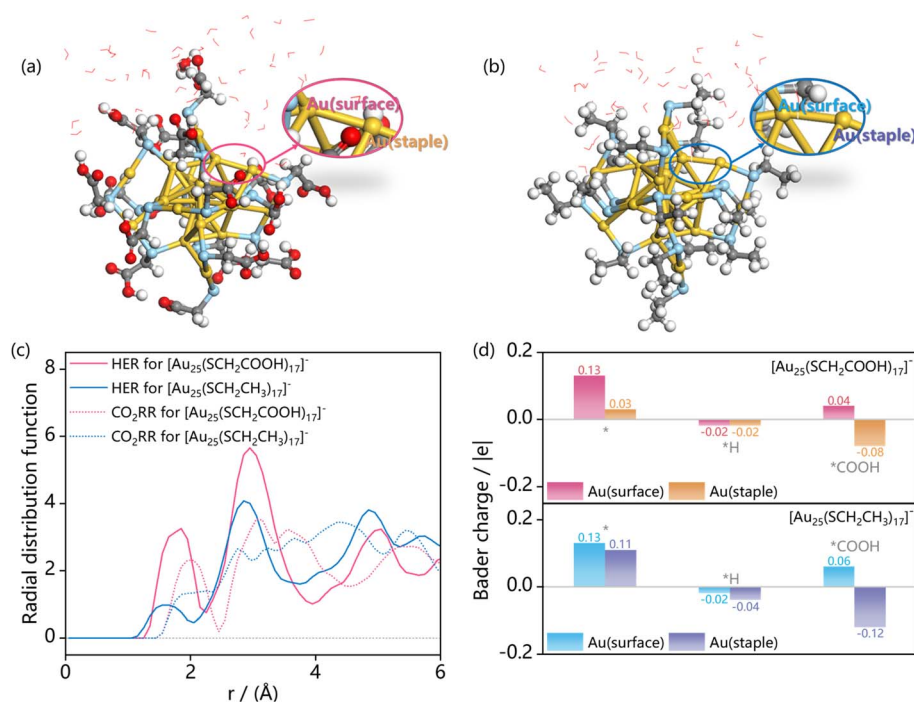

Fig. 4 Local structures of the Au(surface) and Au(staple) sites in (a) $[Au_{25}(SCH_2COOH)_{17}]^-$ and (b) $[Au_{25}(SCH_2CH_3)_{17}]^-$ NCs. (c) Radial distribution function (RDF) of Au active sites with hydrogen atoms from surrounding H_2O during the kinetic process of the rate-determining steps in the HER (solid lines) and CO_2RR (dashed lines) for $[Au_{25}(SCH_2COOH)_{17}]^-$ and $[Au_{25}(SCH_2CH_3)_{17}]^-$. (d) Bader charge analysis of Au(surface) and Au(staple) sites in the NC catalysts before and after the adsorption of key *H and *COOH intermediates in acidic HER and alkaline CO_2RR.

has a significantly lower charge (0.03) compared to $[Au_{25}(SCH_2CH_3)_{17}]^-$ (0.11). The lower charge on Au(staple) in the hydrophilic cluster suggests a lower electron density, which could promote better interaction with protons facilitating proton transfer and enhancing the hydrogen evolution. When hydrogen is adsorbed (*H state), both systems exhibit negative charges on the Au sites, indicating electron transfer from H to Au. However, the Au(staple) site in $[Au_{25}(SCH_2CH_3)_{17}]^-$ holds a higher negative charge (-0.04) compared to $[Au_{25}(SCH_2COOH)_{17}]^-$ (-0.02), suggesting a stronger electron interaction with hydrogen. This stronger interaction likely hinders H_2 desorption in the hydrophobic cluster, increasing the energy barrier for H_2 release. In contrast, the more balanced electron distribution in the hydrophilic cluster allows for easier H_2 desorption, contributing to its superior HER performance. In the *COOH state, a crucial intermediate for the CO_2RR, the Au(staple) in $[Au_{25}(SCH_2CH_3)_{17}]^-$ shows a more negative charge (-0.12) than in $[Au_{25}(SCH_2COOH)_{17}]^-$ (-0.08). This indicates that the hydrophobic cluster better stabilizes the *COOH intermediate by receiving more electrons from the adsorbed species. This enhanced stabilization lowers the energy barrier for *COOH reduction to *CO, explaining the superior CO_2RR performance of $[Au_{25}(SCH_2CH_3)_{17}]^-$. Conversely, the less negative charge on Au(staple) in the hydrophilic cluster results in weaker stabilization of *COOH, leading to a higher energy barrier for this reduction step and contributing to its lower CO_2RR efficiency.

Fig. 5 illustrates the projected density of states (PDOS) and corresponding d-band centers (ε_d) of active Au sites for $[Au_{25}(SCH_2COOH)_{17}]^-$ and $[Au_{25}(SCH_2CH_3)_{17}]^-$ NCs, along with their key intermediates involved in the HER and CO_2RR. The ε_d values offer valuable insights into the electronic properties of these catalysts and their interaction with reaction intermediates. In the pristine nanocluster (* state), $[Au_{25}(SCH_2COOH)_{17}]^-$ exhibits an ε_d of -3.34 eV, while $[Au_{25}(SCH_2CH_3)_{17}]^-$ has a more negative ε_d of -3.61 eV. A more negative ε_d typically indicates a lower energy of the d-band center, which correlates with stronger binding of adsorbates. For the *H state, $[Au_{25}(SCH_2COOH)_{17}]^-$ has an ε_d of -3.14 eV, whereas $[Au_{25}(SCH_2CH_3)_{17}]^-$ shows a more negative ε_d of -3.38 eV. This stronger interaction in $[Au_{25}(SCH_2CH_3)_{17}]^-$ reflects tighter hydrogen binding, which could make H_2 desorption more difficult and increase the energy barrier for the HER. In contrast, the weaker interaction in $[Au_{25}(SCH_2COOH)_{17}]^-$ facilitates easier H_2 desorption, contributing to its superior HER activity. In the *COOH state, the ε_d for $[Au_{25}(SCH_2COOH)_{17}]^-$ is -3.65 eV, compared to a more negative ε_d of -3.78 eV for $[Au_{25}(SCH_2CH_3)_{17}]^-$. The more negative ε_d in $[Au_{25}(SCH_2CH_3)_{17}]^-$ indicates stronger stabilization of the *COOH intermediate, lowering the energy barrier for *COOH to *CO conversion and enhancing the CO_2RR performance.

In summary, our above theoretical analysis revealed that the catalytic differences between $[Au_{25}(SCH_2COOH)_{17}]^-$ and $[Au_{25}(SCH_2CH_3)_{17}]^-$ in the HER and CO_2RR are contributed both by their surface interaction with the water environment and their electronic properties. The RDF analysis shows that $[Au_{25}(SCH_2COOH)_{17}]^-$ with hydrophilic ligands enhances

proton transfer and H_2 desorption, leading to better HER performance. In contrast, the hydrophobic nature of $[Au_{25}(SCH_2CH_3)_{17}]^-$ reduces water interaction and lowers the HER efficiency. The Bader charge and d-band center analyses reveal that $[Au_{25}(SCH_2CH_3)_{17}]^-$ strongly stabilizes the *COOH intermediate, lowering the energy barrier for *CO formation, thereby excelling in the CO_2RR, while $[Au_{25}(SCH_2COOH)_{17}]^-$ shows weaker stabilization of *COOH, leading to higher CO_2RR barriers.

Experimental validation

To validate the computational findings, which indicate that the hydrophilic ligand-protected Au_{25} cluster exhibits superior HER performance in an acidic environment, whereas the hydrophobic ligand-protected Au_{25} cluster excels in the CO_2RR in an alkaline environment, we conducted further experimental investigations. Specifically, we synthesized $[Au_{25}(MPA)_{18}]^-$ as the hydrophilic model and $[Au_{25}(SC_6H_{13})_{18}]^-$ as its hydrophobic counterpart. To confirm the successful synthesis of $[Au_{25}(MPA)_{18}]^-$ and $[Au_{25}(SC_6H_{13})_{18}]^-$ NCs, we conducted the UV-Vis absorption spectroscopy measurements. The UV-Vis spectra of the two Au_{25} NCs, provided in Fig. S10a and b,† exhibit distinct absorption peaks at 400 nm, 450 nm, and 670 nm, which are consistent with the characteristic optical behavior of Au_{25} NCs reported in previous studies.[22,25]

In the HER experiments conducted in 0.5 M H_2SO_4 (Fig. 6a), $[Au_{25}(MPA)_{18}]^-$ demonstrated a lower overpotential of 445 mV at a current density of 10 mA cm^{-2} compared to 541 mV for $[Au_{25}(SC_6H_{13})_{18}]^-$, indicating an enhanced hydrogen evolution activity of the $[Au_{25}(MPA)_{18}]^-$ NC. Additionally, the Tafel slope for $[Au_{25}(MPA)_{18}]^-$ was slightly lower (106 mV dec^{-1}) than that of $[Au_{25}(SC_6H_{13})_{18}]^-$ (111 mV dec^{-1}), suggesting faster reaction kinetics (Fig. 6b). The stability tests over 8.5 hours of continuous operation (Fig. 6c) revealed that $[Au_{25}(MPA)_{18}]^-$ maintained a stable current density, whereas $[Au_{25}(SC_6H_{13})_{18}]^-$ exhibited a reduction of about 10% in the current density, indicating that the hydrophilic $[Au_{25}(MPA)_{18}]^-$ is more stable under acidic HER conditions.

For the CO_2RR performance evaluation, linear sweep voltammetry (LSV) was performed using a CO_2 flow cell with 1.0 M KOH electrolyte. As shown in Fig. 7a, the current density difference between CO_2-saturated and N_2-saturated electrolytes for $[Au_{25}(SC_6H_{13})_{18}]^-$ was larger than that for $[Au_{25}(MPA)_{18}]^-$, indicating that $[Au_{25}(SC_6H_{13})_{18}]^-$ is more favorable for CO_2 reduction to CO. The faradaic efficiency for CO (FE_{CO}) at various potentials (Fig. 7b) showed that $[Au_{25}(SC_6H_{13})_{18}]^-$ achieved a higher FE_{CO}, reaching 97.64% at -0.48 V. In terms of the partial current density for CO production (j_{CO}) (Fig. 7c), $[Au_{25}(MPA)_{18}]^-$ exhibited slightly higher values in the potential range of -0.18 V to -0.48 V, whereas $[Au_{25}(SC_6H_{13})_{18}]^-$ outperformed in the lower potential range of -0.58 V to -0.98 V. The Tafel slopes (Fig. S11†) further indicated the faster reaction kinetics for $[Au_{25}(SC_6H_{13})_{18}]^-$ (199 mV dec^{-1}) than that for $[Au_{25}(MPA)_{18}]^-$ (242 mV dec^{-1}). Additionally, the turnover frequency (TOF) values (Fig. 7d) showed that $[Au_{25}(MPA)_{18}]^-$ has slightly higher TOF between -0.18 V and -0.48 V, while
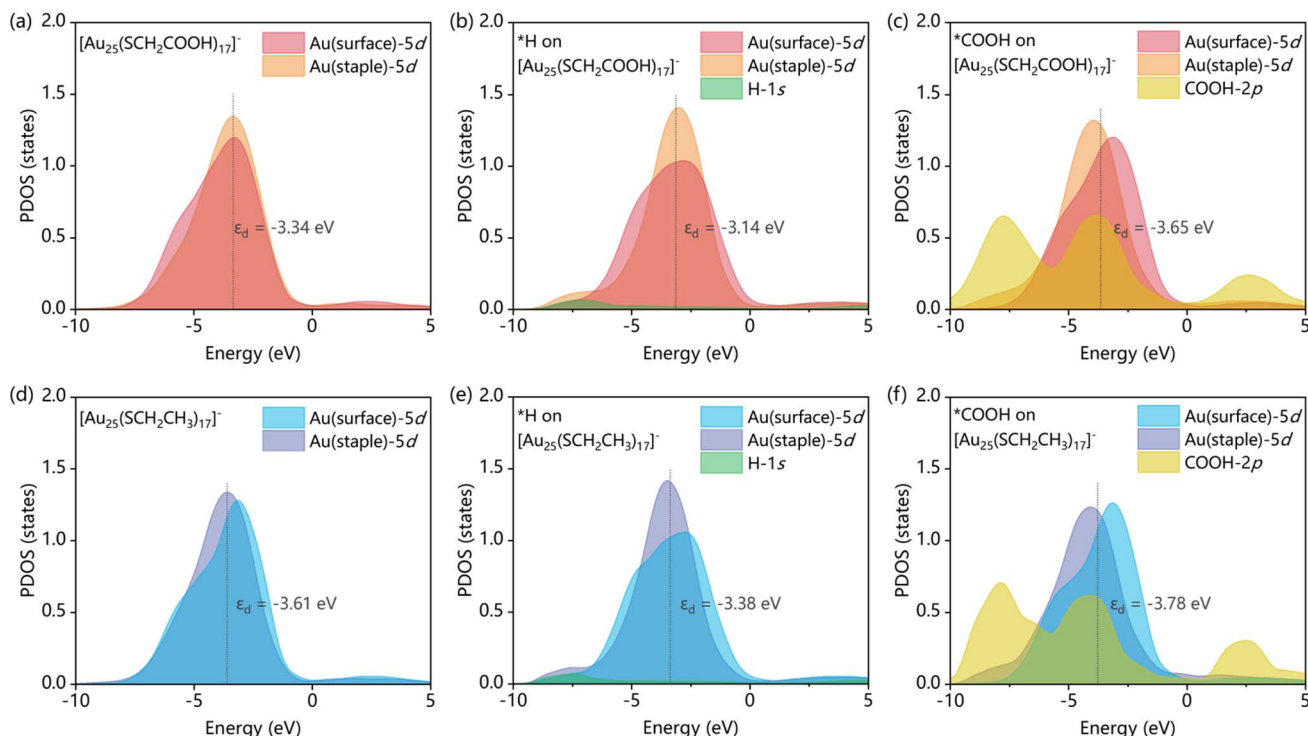
Fig. 5 PDOS and corresponding d-band centers (ε_d) for $[Au_{25}(SCH_2COOH)_{17}]^-$ and $[Au_{25}(SCH_2CH_3)_{17}]^-$, and their key intermediates. (a) $[Au_{25}(SCH_2COOH)_{17}]^-$, (b) *H adsorbed on $[Au_{25}(SCH_2COOH)_{17}]^-$, (c) *COOH adsorbed on $[Au_{25}(SCH_2COOH)_{17}]^-$, (d) $[Au_{25}(SCH_2CH_3)_{17}]^-$, (e) *H adsorbed on $[Au_{25}(SCH_2CH_3)_{17}]^-$, and (f) *COOH adsorbed on $[Au_{25}(SCH_2CH_3)_{17}]^-$.

$[Au_{25}(SC_6H_{13})_{18}]^-$ exhibits significantly higher TOF values from −0.58 V to −0.98 V, indicating the much enhanced activity in lower potential ranges. The long-term stability tests over 8.5 hours of continuous operation demonstrated that $[Au_{25}(MPA)_{18}]^-$ showed a slight decrease of around 4% in FE_{CO} and current density (Fig. 7e), whereas $[Au_{25}(SC_6H_{13})_{18}]^-$ maintained the stable FE_{CO} and current density (Fig. 7f), suggesting that the hydrophobic nanocluster is more stable under alkaline CO_2RR conditions.

Recognizing that the difference in the ligand chain length could also influence the electrocatalytic activity, we further synthesized and tested Au_{25} clusters protected by ligands with similar chain lengths. Specifically, $[Au_{25}(MHA)_{18}]^-$ (MHA = 6-mercaptohexanoic acid) was chosen as a hydrophilic analog with

a chain length comparable to that of $[Au_{25}(SC_6H_{13})_{18}]^-$. These additional experiments, detailed in the ESI,† provide a comprehensive analysis of how both ligand hydrophilicity and chain length affect the catalytic performance of Au_{25} NCs. The UV-Vis spectra of the synthesized $[Au_{25}(MHA)_{18}]^-$ NCs exhibit distinct absorption peaks at 400 nm, 450 nm, and 670 nm (Fig. S10c†), confirming the successful synthesis of Au_{25} NCs.[21,22,25]

The LSV curves were measured in a flow cell with 1.0 M KOH electrolyte (Fig. S12a†), revealing that $[Au_{25}(SC_6H_{13})_{18}]^-$ NCs are more favorable for CO_2 reduction to CO. In the comparison of FE_{CO} at various potentials (Fig. S12b†), $[Au_{25}(SC_6H_{13})_{18}]^-$ NCs demonstrate higher CO_2 reduction selectivity than $[Au_{25}(MHA)_{18}]^-$ NCs, with the maximum FE_{CO} for $[Au_{25}(MHA)_{18}]^-$ reaching only 88%. As shown in Fig. S12c,† the

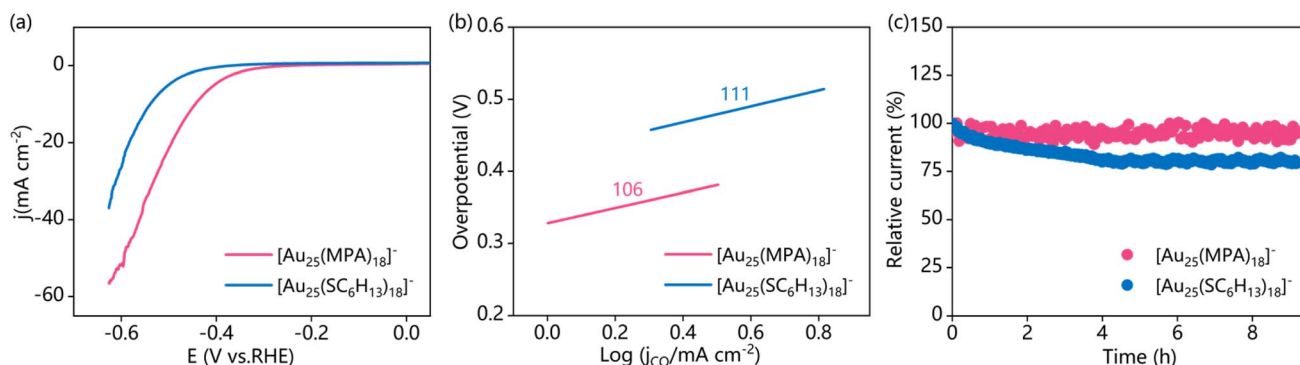**Fig. 6** Electrocatalytic HER performance in 0.5 M H_2SO_4. (a) LSV curves of $[Au_{25}(MPA)_{18}]^-$ and $[Au_{25}(SC_6H_{13})_{18}]^-$. (b) Tafel slopes of the catalysts. (c) Chronoamperometric plots at 10 mA cm^{-2} for the HER stability testing.
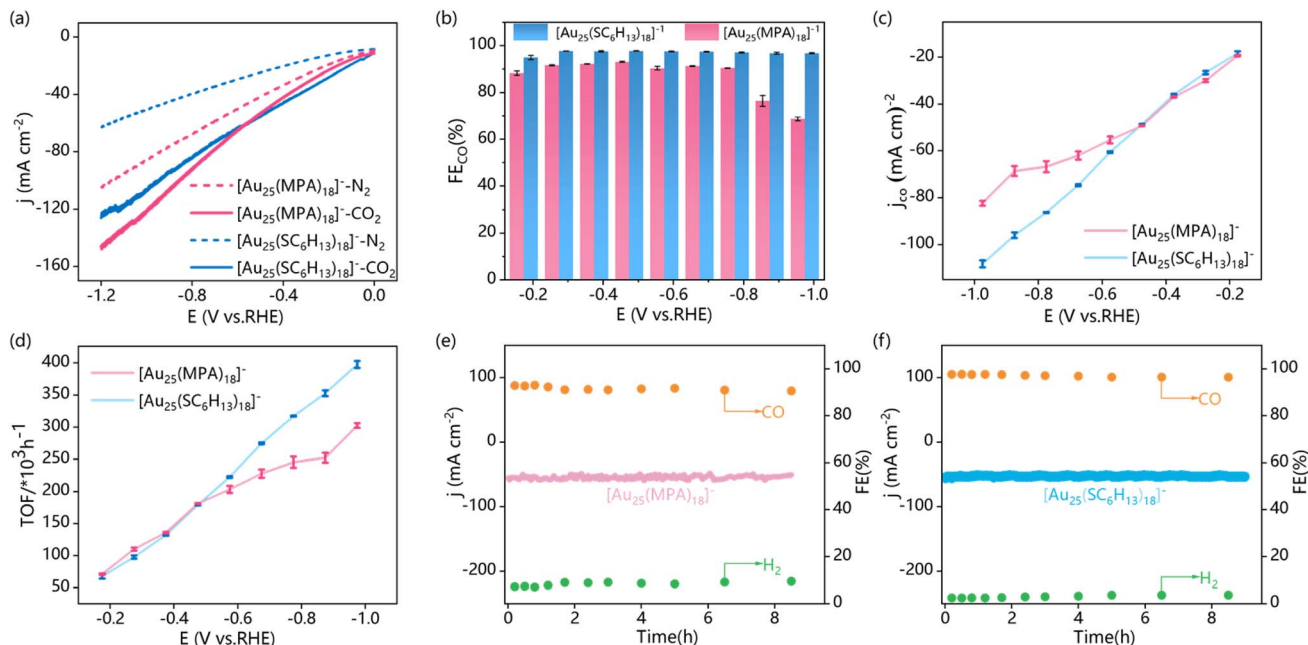
Fig. 7 Electrocatalytic CO₂RR performance in a CO₂ flow cell with 1 M KOH electrolyte. (a) LSV curves of $[Au_{25}(MPA)_{18}]^-$ and $[Au_{25}(SC_6H_{13})_{18}]^-$ in N_2 and CO_2 environments. (b) Faradaic efficiency for CO (FE_{CO}) of $[Au_{25}(MPA)_{18}]^-$ and $[Au_{25}(SC_6H_{13})_{18}]^-$ at different potentials. (c) Fractional current density of CO at various potentials. (d) Turnover frequency (TOF) of CO at different potentials. (e and f) Long-term stability tests of $[Au_{25}(MPA)_{18}]^-$ and $[Au_{25}(SC_6H_{13})_{18}]^-$ for the CO₂RR at −0.48 V.

j_{CO} of $[Au_{25}(SC_6H_{13})_{18}]^-$ NCs is up to twice as high as that of $[Au_{25}(MHA)_{18}]^-$ NCs. The Tafel slopes (Fig. S13†) further highlight the faster reaction kinetics for $[Au_{25}(SC_6H_{13})_{18}]^-$ NCs (199 mV dec^{-1}) compared to $[Au_{25}(MHA)_{18}]^-$ (498 mV dec^{-1}). Additionally, the TOF values (Fig. S12d†) indicate that $[Au_{25}(SC_6H_{13})_{18}]^-$ exhibits significantly higher TOF than $[Au_{25}(MHA)_{18}]^-$ across various potentials.

These experimental results have well corroborated our computational predictions, confirming that the hydrophilic ligand-protected Au₂₅ NCs are more effective for the HER in acidic environments due to enhanced proton transfer facilitated by the hydrophilic ligands. Conversely, the hydrophobic ligand-protected Au₂₅ NCs demonstrate superior CO₂RR activity under alkaline conditions by promoting adsorption of CO₂RR intermediates and minimizing the water interference, thereby enhancing CO₂ reduction efficiency. Further experiments with ligands of similar chain lengths to the hydrophilic and hydrophobic Au₂₅ NCs reveal that both ligand hydrophilicity and chain length influence catalytic performance. However, the hydrophilicity of the ligands plays a dominant role in determining the overall catalytic behavior. This alignment between computational and experimental findings underscores the critical role of ligand properties in tuning the electrocatalytic performance of atomically precise metal NCs, providing valuable insights for the rational ligand design of nanocatalysts in sustainable energy applications.

3. Conclusion

In this study, we have systematically explored how the ligand hydrophilicity and hydrophobicity influence the interface dynamics and the electrocatalytic performance of Au₂₅ NCs in important reactions such as the HER and CO₂RR. Our computations revealed that the hydrophilic $[Au_{25}(SCH_2COOH)_{17}]^-$ NC exhibits faster breakage of the Au–S bond and desorption of the thiolate ligand into solution at the applied reduction potential. The dethiolated $[Au_{25}(SCH_2COOH)_{17}]^-$ NC is predicted to exhibit superior acid HER activity due to enhanced proton transfer and efficient hydrogen evolution facilitated by stronger hydrogen bond interactions with water molecules. Conversely, the hydrophobic $[Au_{25}(SCH_2CH_3)_{17}]^-$ NC demonstrates enhanced alkaline CO₂RR performance by stabilizing key CO₂RR intermediates and minimizing the water interference to lower the barrier for CO formation. The electrochemical experiments using synthesized $[Au_{25}(MPA)_{18}]^-$ and $[Au_{25}(SC_6H_{13})_{18}]^-$ as models, which have similar ligand molecular weights, have further validated our predictions. Hydrophilic $[Au_{25}(MPA)_{18}]^-$ showed better activity, lower overpotential, and greater stability in the acidic HER testing, while hydrophobic $[Au_{25}(SC_6H_{13})_{18}]^-$ achieved higher faradaic efficiency, current density, and stability in alkaline CO₂RR. Moreover, the results from clusters with similar chain lengths, such as $[Au_{25}(MHA)_{18}]^-$ and $[Au_{25}(SC_6H_{13})_{18}]^-$, further corroborated our computations, highlighting that both ligand hydrophilicity and chain length influence the catalytic performance, with hydrophilicity being the dominant factor in determining the overall catalytic behavior. These results not only provide an atomic level understanding of the ligand effects on the interface dynamics and electrocatalytic performance of metal NCs, but also stimulate ligand engineering as a facile strategy to optimize the catalytic activity of nanocluster catalysts for specific catalytic targets in future electrocatalysis research.

4. Computational methods and experimental section

Ligand removal dynamics

The dynamics of ligand removal from the nanocluster were investigated using the CP2K package (version 2023.1).[50] The simulations employed the Perdew–Burke–Ernzerhof (PBE) functional within the generalized gradient approximation (GGA) in combination with the hybrid Gaussian/Plane-Wave (GPW) scheme.[51] The computational domain was defined with a periodic lattice size of $23 \times 23 \times 28$ Å^3, including 192 water molecules to simulate the solvent environment. Molecular dynamics (MD) simulations were performed in the canonical (NVT) ensemble using Nose–Hoover thermostats to maintain a constant temperature of 300 K.[52,53] A time step of 1.0 fs was used throughout the simulations, which were run for a total of 10 ps. Dispersion corrections were applied using the DFT-D3 method to account for van der Waals interactions.[54,55] The electronic structure was described by density functional theory (DFT) with spin-polarization and a mixed double-ζ Gaussian and plane-wave basis set, with an energy cutoff of 400 Ry.[56]

Thermodynamic calculations for the HER and CO$_2$RR

Spin-polarized DFT calculations were carried out using the Vienna Ab initio Simulation Package (VASP, version 5.4.4).[57] The exchange–correlation effects were described using the Perdew–Burke–Ernzerhof (PBE) functional within the generalized gradient approximation (GGA).[51] The projector-augmented wave (PAW) method was employed to account for electron–ion interactions with a cutoff energy of 400 eV.[58] For these calculations, the computational cell was set with a lattice size of $23 \times 23 \times 28$ Å^3, including 50 water molecules to adapt to the specific requirements of the reaction environments. The empirical DFT-D3 dispersion correction was applied to include van der Waals interactions.[59] Brillouin zone integration was performed using a gamma centered $1 \times 1 \times 1$ k-point grid, with convergence criteria set at 0.05 eV Å^{-1} for forces and 10^{-4} eV per cell for energy. The electrode potential was determined via tuning the work function (additional details are provided in the ESI†).

Dynamic calculations for the HER and CO$_2$RR

Ab initio molecular dynamics (AIMD) simulations were conducted using the Nose–Hoover thermostat in the canonical (NVT) ensemble at 300 K with a time step of 1 fs.[52,60] Thermodynamic integrations and the "slow-growth" method were employed to derive the free energy profiles for the rate-determining steps in the HER and CO$_2$RR. The collective variable (CV) increment was set to 0.0008 Å, and the simulation time was 3 ps. Reaction barriers and reaction energies were determined by integrating the free-energy gradients to generate the free energy profiles.[61,62]

Chemicals and materials

Tetrachloroauric(III) acid (HAuCl$_4\cdot$3H$_2$O, >99.99%), tetraoctylammonium bromide (TOAB, 98%), 1-hexanethiol (97%), 3-mercaptopropionic acid (MPA, 98%), 6-mercaptohexanoic acid (MHA, 98%), sodium borohydride (NaBH$_4$), sodium hydroxide (NaOH), potassium hydroxide (KOH), Nafion solution (5 wt%), and solvents: reverse osmosis water, methanol, ethanol, acetonitrile (CH$_3$CN), dichloromethane (CH$_2$Cl$_2$) and tetrahydrofuran (THF) were used. High purity (>99.999%) Ar and CO$_2$ gases were used.

Preparation of the [Au$_{25}$(MPA)$_{18}$]$^-$ NCs

In a typical synthesis of [Au$_{25}$(MPA)$_{18}$]$^-$ clusters, 4 mg of HAuCl$_4\cdot$3H$_2$O (0.05 mmol) and 2.1 mg of MPA (0.09 mmol) were mixed in 4.7 mL of ultrapure water under mild stirring. Subsequently, 3 mL of NaOH solution (1.0 M) was added, causing the solution color to change from yellow to pale yellow. Then, 1 mL of NaBH$_4$ solution (0.1 M) was added dropwise, turning the solution yellowish-brown. After 3 hours of vigorous stirring, unreacted MPA and other impurities were removed using organic solvents and spin distillation, yielding highly pure MPA-protected Au$_{25}$ nanoclusters.

Preparation of the [Au$_{25}$(MHA)$_{18}$]$^-$ NCs

The procedure of the [Au$_{25}$(MHA)$_{18}$]$^-$ NCs is similar to the synthesis of [Au$_{25}$(MPA)$_{18}$]$^-$. 4.0 mg of HAuCl$_4\cdot$3H$_2$O (0.05 mmol) and 4.0 mL of MHA (50 mM) were mixed in 4.7 mL of ultrapure water under mild stirring. Subsequently, 0.5 mL of NaOH solution (1.0 M) was added, causing the solution color to change from yellow to pale yellow. Then, 1 mL of NaBH$_4$ solution (0.1 M) was added dropwise, turning the solution yellowish-brown. After 2 h of vigorous stirring, the obtained product was purified using organic solvents to remove unreacted MHA and other impurities, yielding [Au$_{25}$(MHA)$_{18}$]$^-$ nanoclusters.

Preparation of the [Au$_{25}$(SC$_6$H$_{13}$)$_{18}$]$^-$ NCs

HAuCl$_4\cdot$3H$_2$O (0.125 mmol) and TOAB (0.145 mmol) were dissolved in 14 mL of THF in a 50 mL vial. After vigorous stirring for 15 minutes, the solution color changed from orange to red. Then, 1-hexanethiol (0.625 mmol) was slowly added, and the mixture was stirred for 1 hour until the red solution turned colorless. Next, freshly prepared NaBH$_4$ (1.25 mmol) in 2 mL of cold water was quickly added, producing bubbles as the solution turned black, indicating the formation of gold clusters. The reaction mixture was stirred for an additional 24 hours. The product was then transferred to a 25 mL round-bottom flask and dried by rotary evaporation. The dried product was redissolved in CH$_2$Cl$_2$, and the supernatant was transferred to another round-bottom flask and dried again by rotary evaporation. Finally, the product was washed with ethanol, collected by centrifugation, and the washing process was repeated at least 10 times to ensure the removal of impurities.

Electrochemical measurements

The electrochemical tests were conducted using a CHI 760E electrochemical workstation (CH Instruments Inc.) at room temperature. For HER testing, cyclic voltammetry (CV) and LSV curves were obtained in a three-electrode cell setup, consisting

of a glassy carbon disk electrode (GCE, diameter 5 mm, surface area 0.07 cm^2) as the working electrode, polished with alumina slurry and cleaned with ethanol and deionized water. A carbon rod served as the counter electrode, and an Ag/AgCl electrode in 0.5 M H_2SO_4 was used as the reference electrode. The potential of the reference electrode was calibrated to the reversible hydrogen electrode (RHE) using the equation: $E_{RHE} = E_{Hg/HgCl_2} + (0.244 + 0.0591 \times pH)$ V in 0.5 M H_2SO_4 solution. The working electrode for the HER was prepared by dissolving 1 mg of carbon nanotube and 1 mg of Au_{25} NCs in 0.5 mL of CH_2Cl_2, creating an ink with 10 μL of 5 wt% Nafion. Before testing, 3.5 μL of the catalyst and 3 μL of Nafion (5 wt%) were cast onto the GCE.

The catalytic activity of Au_{25} NCs in the CO$_2$RR was determined using an electrochemical workstation (CHI 600E) with a three-electrode system coupled to a CO_2 flow cell. The electrolyte solution was 1 M KOH, and the reference electrode was an Ag/AgCl electrode immersed in saturated KCl solution. An anion-exchange membrane and a platinum plate were used as the ion mobility channel and counter electrode, respectively. The working electrode was prepared by dissolving 1 mg of carbon nanotube and 1 mg of Au_{25} NCs in 0.5 mL of CH_2Cl_2, creating a uniform dispersion ink containing 10 μL of 5 wt% Nafion solution. This solution was sprayed onto a 1 cm^2 gas diffusion layer (GDL) with a mass loading of 2 mg cm^{-2}. The potentials were converted to the RHE using the following equation:

$$E(RHE) = E(Ag/AgCl) + 0.197 \text{ V} + 0.0591 \times pH$$

Before the electrochemical CO_2 reduction reaction, the cathodic electrolyte was saturated with CO_2 for 30 minutes. The cathodic and anodic reaction chambers were separated using an anion exchange membrane. During the CO$_2$RR process, each electrolyte cell contained 30 mL of electrolyte, circulated at 40 rpm using a peristaltic pump. The gas products were analyzed quantitatively with a gas chromatograph (GC, Huaai 9560). The faradaic efficiency (FE) of the gas products was calculated using the formula:

$$FE = \frac{Q_i}{Q_{total}} = \frac{N_i \times Z \times F}{Q_{total}}$$

where Q_i is the charge required to form the gaseous product, Q_{total} is the total charge during the reaction, N_i is the number of moles of the product detected by gas chromatography, Z is the number of electrons transferred during the formation of the product (2 for CO and H_2), and F is Faraday's constant (96 485 C mol^{-1}).

The turnover frequency (TOF) was calculated as follows:

$$TOF(h^{-1}) = \frac{j_i/ZF}{m_i \times \omega/M} \times 3600$$

where j_i is the partial current density of the corresponding gas product, Z is the number of transferred electrons during the formation of the product (2 for CO), F is the Faraday constant (96 485 C mol^{-1}), m_i is the mass of the loaded catalyst, ω is the

relative mass fraction of Au in the catalyst, and M is the relative atomic mass of Au. Linear sweep voltammetry (LSV) was conducted in a 1 M KOH solution saturated with either N_2 or CO_2, using a scan rate of 50 mV s^{-1}.

Data availability

The data supporting this article have been included as part of the ESI.†

Author contributions

Q. T. conceived the idea. L. L. performed the theoretical calculations with help from Y. C. and F. S. X. Z. performed the experiments and analyzed the data under the guidance of L. W. L. L. wrote the manuscript with inputs from all authors. Q. T. and L. W. finalized the manuscript. All the authors approved the final version of the manuscript.

Conflicts of interest

The authors declare no competing financial interests.

Acknowledgements

References

1 Z. Zhou, Z. Pei, L. Wei, S. Zhao, X. Jian and Y. Chen, Electrocatalytic hydrogen evolution under neutral pH conditions: current understandings, recent advances, and future prospects, *Energy Environ. Sci.*, 2020, **13**, 3185–3206.

2 W. Zhai, Y. Ma, D. Chen, J. C. Ho, Z. Dai and Y. Qu, Recent progress on the long-term stability of hydrogen evolution reaction electrocatalysts, *InfoMat*, 2022, **4**, e12357.

3 L. Xiong, Y. Qiu, X. Peng, Z. Liu and P. K. Chu, Electronic structural engineering of transition metal-based electrocatalysts for the hydrogen evolution reaction, *Nano Energy*, 2022, **104**, 107882.

4 M. Ďurovič, J. Hnát and K. Bouzek, Electrocatalysts for the hydrogen evolution reaction in alkaline and neutral media. A comparative review, *J. Power Sources*, 2021, **493**, 229708.

5 X. Zhang, S.-X. Guo, K. A. Gandionco, A. M. Bond and J. Zhang, Electrocatalytic carbon dioxide reduction: from fundamental principles to catalyst design, *Mater. Today Adv.*, 2020, **7**, 100074.

6 T. Ahmad, S. Liu, M. Sajid, K. Li, M. Ali, L. Liu and W. Chen, Electrochemical CO_2 reduction to C$_{2+}$ products using Cu-based electrocatalysts: a review, *Nano Res. Energy*, 2022, **1**, e9120021.

7 D. Xu, K. Li, B. Jia, W. Sun, W. Zhang, X. Liu and T. Ma, Electrocatalytic CO_2 reduction towards industrial applications, *Carbon Energy*, 2023, **5**, e230.

8   X. An, S. Li, X. Hao, Z. Xie, X. Du, Z. Wang, X. Hao, A. Abudula and G. Guan, Common strategies for improving the performances of tin and bismuth-based catalysts in the electrocatalytic reduction of CO_2 to formic acid/formate, *Renewable Sustainable Energy Rev.*, 2021, **143**, 110952.

9   X. Mao, W. Gong, Y. Fu, J. Li, X. Wang, A. P. O'Mullane, Y. Xiong and A. Du, Computational Design and Experimental Validation of Enzyme Mimicking Cu-Based Metal–Organic Frameworks for the Reduction of CO_2 into C_2 Products: C–C Coupling Promoted by Ligand Modulation and the Optimal Cu–Cu Distance, *J. Am. Chem. Soc.*, 2023, **145**, 21442–21453.

10 K. Sokołowska, S. Malola, M. Lahtinen, V. Saarnio, P. Permi, K. Koskinen, M. Jalasvuori, H. Häkkinen, L. Lehtovaara and T. Lahtinen, Towards controlled synthesis of water-soluble gold nanoclusters: synthesis and analysis, *J. Phys. Chem. C*, 2019, **123**, 2602–2612.

11 P. Maity, S. Xie, M. Yamauchi and T. Tsukuda, Stabilized gold clusters: from isolation toward controlled synthesis, *Nanoscale*, 2012, **4**, 4027–4037.

12 K. Kwak and D. Lee, Electrochemistry of atomically precise metal nanoclusters, *Acc. Chem. Res.*, 2018, **52**, 12–22.

13 Y. Jo, M. Choi, M. Kim, J. S. Yoo, W. Choi and D. Lee, Promotion of alkaline hydrogen production *via* Ni-doping of atomically precise Ag nanoclusters, *Bull. Korean Chem. Soc.*, 2021, **42**, 1672–1677.

14 S. Zhao, R. Jin and R. Jin, Opportunities and challenges in CO_2 reduction by gold-and silver-based electrocatalysts: from bulk metals to nanoparticles and atomically precise nanoclusters, *ACS Energy Lett.*, 2018, **3**, 452–462.

15 Q. Tang, G. Hu, V. Fung and D.-e. Jiang, Insights into interfaces, stability, electronic properties, and catalytic activities of atomically precise metal nanoclusters from first principles, *Acc. Chem. Res.*, 2018, **51**, 2793–2802.

16 F. Sun, C. Deng, S. Tian and Q. Tang, Oxygen electrocatalysis by $[Au_{25}(SR)_{18}]$: charge, doping, and ligand removal effect, *ACS Catal.*, 2021, **11**, 7957–7969.

17 F. Sun, Q. Tang and D.-e. Jiang, Theoretical advances in understanding and designing the active sites for hydrogen evolution reaction, *ACS Catal.*, 2022, **12**, 8404–8433.

18 T. Kawawaki, T. Okada, D. Hirayama and Y. Negishi, Atomically precise metal nanoclusters as catalysts for electrocatalytic CO_2 reduction, *Green Chem.*, 2024, **26**, 122–163.

19 W. Choi, H. Seong, V. Efremov, Y. Lee, S. Im, D.-H. Lim, J. S. Yoo and D. Lee, Controlled syngas production by electrocatalytic CO_2 reduction on formulated $Au_{25}(SR)_{18}$ and $PtAu_{24}(SR)_{18}$ nanoclusters, *J. Chem. Phys.*, 2021, **155**, 014305.

20 D. R. Alfonso, D. Kauffman and C. Matranga, Active sites of ligand-protected Au_{25} nanoparticle catalysts for CO_2 electroreduction to CO, *J. Chem. Phys.*, 2016, **144**, 184705.

21 H. Seong, V. Efremov, G. Park, H. Kim, J. S. Yoo and D. Lee, Atomically precise gold nanoclusters as model catalysts for identifying active sites for electroreduction of CO_2, *Angew. Chem.*, 2021, **133**, 14684–14691.

22 S. M. Han, M. Park, J. Kim and D. Lee, Boosting the Electroreduction of CO_2 to CO by Ligand Engineering of Gold Nanoclusters, *Angew. Chem.*, 2024, **63**, e202404387.

23 O. López-Estrada, N. Mammen, L. Laverdure, M. M. Melander, H. Häkkinen and K. Honkala, Computational Criteria for Hydrogen Evolution Activity on Ligand-Protected Au_{25}-Based Nanoclusters, *ACS Catal.*, 2023, **13**, 8997–9006.

24 Y. Li, S. Li, A. V. Nagarajan, Z. Liu, S. Nevins, Y. Song, G. Mpourmpakis and R. Jin, Hydrogen evolution electrocatalyst design: turning inert gold into active catalyst by atomically precise nanochemistry, *J. Am. Chem. Soc.*, 2021, **143**, 11102–11108.

25 K. Kwak, W. Choi, Q. Tang, D.-e. Jiang and D. Lee, Rationally designed metal nanocluster for electrocatalytic hydrogen production from water, *J. Mater. Chem. A*, 2018, **6**, 19495–19501.

26 G. Hu, Q. Tang, D. Lee, Z. Wu and D.-e. Jiang, Metallic hydrogen in atomically precise gold nanoclusters, *Chem. Mater.*, 2017, **29**, 4840–4847.

27 F. Sun, L. Qin, Z. Tang and Q. Tang, Revisiting the activity origin of the $PtAu_{24}(SR)_{18}$ nanocluster for enhanced electrocatalytic hydrogen evolution by combining first-principles simulations with the experimental *in situ* FTIR technique, *Chem. Sci.*, 2024, **15**, 16142–16155.

28 D. R. Kauffman, D. Alfonso, C. Matranga, H. Qian and R. Jin, Experimental and computational investigation of Au_{25} clusters and CO_2: a unique interaction and enhanced electrocatalytic activity, *J. Am. Chem. Soc.*, 2012, **134**, 10237–10243.

29 K. Kwak, W. Choi, Q. Tang, M. Kim, Y. Lee, D.-e. Jiang and D. Lee, A molecule-like $PtAu_{24}(SC_6H_{13})_{18}$ nanocluster as an electrocatalyst for hydrogen production, *Nat. Commun.*, 2017, **8**, 14723.

30 E. Pensa, L. M. Azofra, R. C. Salvarezza and P. Carro, Effect of ligands on the stability of gold nanoclusters, *J. Phys. Chem. Lett.*, 2022, **13**, 6475–6480.

31 S. Li, A. V. Nagarajan, Y. Li, D. R. Kauffman, G. Mpourmpakis and R. Jin, The role of ligands in atomically precise nanocluster-catalyzed CO_2 electrochemical reduction, *Nanoscale*, 2021, **13**, 2333–2337.

32 B. Kumar, T. Kawawaki, N. Shimizu, Y. Imai, D. Suzuki, S. Hossain, L. V. Nair and Y. Negishi, Gold nanoclusters as electrocatalysts: size, ligands, heteroatom doping, and charge dependences, *Nanoscale*, 2020, **12**, 9969–9979.

33 S. F. Yuan, R. L. He, X. S. Han, J. Q. Wang, Z. J. Guan and Q. M. Wang, Robust gold nanocluster protected with amidinates for electrocatalytic CO_2 reduction, *Angew. Chem., Int. Ed.*, 2021, **60**, 14345–14349.

34 J. Wang, F. Xu, Z. Y. Wang, S. Q. Zang and T. C. Mak, Ligand-Shell Engineering of a Au_{28} Nanocluster Boosts Electrocatalytic CO_2 Reduction, *Angew. Chem., Int. Ed.*, 2022, **61**, e202207492.

35 X. Li, S. Takano and T. Tsukuda, Ligand effects on the hydrogen evolution reaction catalyzed by Au_{13} and $Pt@Au_{12}$: alkynyl *vs.* thiolate, *J. Phys. Chem. C*, 2021, **125**, 23226–23230.

36 J. C. Love, L. A. Estroff, J. K. Kriebel, R. G. Nuzzo and G. M. Whitesides, Self-assembled monolayers of thiolates on metals as a form of nanotechnology, *Chem. Rev.*, 2005, **105**, 1103–1170.

37 C. Vericat, M. Vela, G. Benitez, P. Carro and R. Salvarezza, Self-assembled monolayers of thiols and dithiols on gold: new challenges for a well-known system, *Chem. Soc. Rev.*, 2010, **39**, 1805–1834.

38 R. G. Nuzzo and D. L. Allara, Adsorption of bifunctional organic disulfides on gold surfaces, *J. Am. Chem. Soc.*, 1983, **105**, 4481–4483.

39 Z. Liu, H. Tan, B. Li, Z. Hu, D.-e. Jiang, Q. Yao, L. Wang and J. Xie, Ligand effect on switching the rate-determining step of water oxidation in atomically precise metal nanoclusters, *Nat. Commun.*, 2023, **14**, 3374.

40 S. Yoo, S. Yoo, G. Deng, F. Sun, K. Lee, H. Jang, C. W. Lee, X. Liu, J. Jang, Q. Tang, Y. J. Hwang, T. Hyeon and M. S. Bootharaju, Nanocluster surface microenvironment modulates electrocatalytic CO_2 reduction, *Adv. Mater.*, 2024, **36**, 2313032.

41 S. Zhao, N. Austin, M. Li, Y. Song, S. D. House, S. Bernhard, J. C. Yang, G. Mpourmpakis and R. Jin, Influence of atomic-level morphology on catalysis: the case of sphere and rod-like gold nanoclusters for CO_2 electroreduction, *ACS Catal.*, 2018, **8**, 4996–5001.

42 N. Austin, S. Zhao, J. R. McKone, R. Jin and G. Mpourmpakis, Elucidating the active sites for CO_2 electroreduction on ligand-protected Au_{25} nanoclusters, *Catal. Sci. Technol.*, 2018, **8**, 3795–3805.

43 S. Li, D. Alfonso, A. V. Nagarajan, S. D. House, J. C. Yang, D. R. Kauffman, G. Mpourmpakis and R. Jin, Monopalladium substitution in gold nanoclusters enhances CO_2 electroreduction activity and selectivity, *ACS Catal.*, 2020, **10**, 12011–12016.

44 S. Li, A. V. Nagarajan, D. R. Alfonso, M. Sun, D. R. Kauffman, G. Mpourmpakis and R. Jin, Boosting CO_2 electrochemical reduction with atomically precise surface modification on gold nanoclusters, *Angew. Chem., Int. Ed.*, 2021, **60**, 6351–6356.

45 R. Jin, Quantum sized, thiolate-protected gold nanoclusters, *Nanoscale*, 2010, **2**, 343–362.

46 P. Hu, L. Chen, X. Kang and S. Chen, Surface functionalization of metal nanoparticles by conjugated metal–ligand interfacial bonds: impacts on intraparticle charge transfer, *Acc. Chem. Res.*, 2016, **49**, 2251–2260.

47 F. Sun, L. Qin, Z. Tang, G. Deng, M. S. Bootharaju, Z. Wei, Q. Tang and T. Hyeon, SR removal or –R removal? A mechanistic revisit on the puzzle of ligand etching of

$Au_{25}(SR)_{18}$ nanoclusters during electrocatalysis, *Chem. Sci.*, 2023, **14**, 10532–10546.

48 T. Giorgino, Computing 1-D atomic densities in macromolecular simulations: the density profile tool for VMD, *Comput. Phys. Commun.*, 2014, **185**, 317–322.

49 X. Zhao and Y. Liu, Origin of selective production of hydrogen peroxide by electrochemical oxygen reduction, *J. Am. Chem. Soc.*, 2021, **143**, 9423–9428.

50 J. VandeVondele, M. Krack, F. Mohamed, M. Parrinello, T. Chassaing and J. Hutter, Quickstep: fast and accurate density functional calculations using a mixed Gaussian and plane waves approach, *Comput. Phys. Commun.*, 2005, **167**, 103–128.

51 J. P. Perdew, K. Burke and M. Ernzerhof, Generalized gradient approximation made simple, *Phys. Rev. Lett.*, 1996, **77**, 3865.

52 W. G. Hoover, Canonical dynamics: equilibrium phase-space distributions, *Phys. Rev. A: At., Mol., Opt. Phys.*, 1985, **31**, 1695.

53 G. J. Martyna, M. L. Klein and M. Tuckerman, Nosé–Hoover chains: the canonical ensemble *via* continuous dynamics, *J. Chem. Phys.*, 1992, **97**, 2635–2643.

54 S. Grimme, J. Antony, S. Ehrlich and H. Krieg, A consistent and accurate *ab initio* parametrization of density functional dispersion correction (DFT-D) for the 94 elements H-Pu, *J. Chem. Phys.*, 2010, **132**, 154104.

55 S. Grimme, S. Ehrlich and L. Goerigk, Effect of the damping function in dispersion corrected density functional theory, *J. Comput. Chem.*, 2011, **32**, 1456–1465.

56 J. VandeVondele and J. Hutter, Gaussian basis sets for accurate calculations on molecular systems in gas and condensed phases, *J. Chem. Phys.*, 2007, **127**, 114105.

57 G. Kresse and J. Furthmüller, Efficient iterative schemes for *ab initio* total-energy calculations using a plane-wave basis set, *Phys. Rev. B: Condens. Matter Mater. Phys.*, 1996, **54**, 11169.

58 P. E. Blöchl, Projector augmented-wave method, *Phys. Rev. B: Condens. Matter Mater. Phys.*, 1994, **50**, 17953.

59 I. L. Garzon and A. Posada-Amarillas, Structural and vibrational analysis of amorphous Au_{55} clusters, *Phys. Rev. B: Condens. Matter Mater. Phys.*, 1996, **54**, 11796.

60 R. W. Hall and B. J. Berne, Nonergodicity in path integral molecular dynamics, *J. Chem. Phys.*, 1984, **81**, 3641–3643.

61 M. Sprik and G. Ciccotti, Free energy from constrained molecular dynamics, *J. Chem. Phys.*, 1998, **109**, 7737–7744.

62 A. A. Hassanali, J. Cuny, V. Verdolino and M. Parrinello, Aqueous solutions: state of the art in *ab initio* molecular dynamics, *Philos. Trans. R. Soc., A*, 2014, **372**, 20120482.